Magnetic field reversals in numerical simulations of the von Kármán sodium experiment

Rémi Bousquet,[1] Yannick Ponty,[2] Victor Botez,[1] Nicolas Plihon,[3] and Caroline Nore[1]
[1]*Université Paris-Saclay, CNRS, Laboratoire Interdisciplinaire des Sciences du Numérique, F-91405 Orsay, France*
[2]*Université de la Côte d'Azur, CNRS, Observatoire de la Côte d'Azur, Boulevard de l'Observatoire CS 34229 06304 Nice Cedex 4, France*
[3]*Université de Lyon, ENS de Lyon, CNRS, Laboratoire de Physique, F-69342 Lyon, France*

(Received 19 January 2026; accepted 29 May 2026; published 18 June 2026)

Numerical simulations and proper orthogonal decomposition are used to identify the fundamental mechanism of magnetic field reversals in the von Kármán sodium experiment with ferromagnetic impellers close to contrarotation. Two numerical solvers are used and agree well on the resulting mechanism. The reversal dynamics rely on the interaction of four dominant axisymmetric modes: the magnetic dipole mode D and quadrupole mode Q, as well as the zonal velocity mode V and the R_π-symmetric mode U. This hierarchy leads to a reduced-order $DQVU$ Galerkin model derived from the magnetohydrodynamic equations. The model improves upon previous three-variable versions by adding a velocity variable U and related interactions, which are shown to be essential for reproducing the main features of magnetic field dynamics.

DOI: 10.1103/9tx2-1m13

I. INTRODUCTION

Magnetic fields of celestial bodies, such as the Earth and the Sun, are generated by dynamo action, which is the self-generation of magnetic fields by the motion of electrically conducting fluids [1,2]. These natural dynamos often display polarity reversals, occurring periodically, as in the case of the solar cycle, or follow a chaotic pattern, as seen in the history of Earth's geomagnetic field. Reversals, excursions, and the weakening of the Earth's magnetic field can have a significant impact on modern technologies [3], making the understanding of these phenomena a critical scientific challenge. Up until this point, except for recent realizations in laser-produced plasmas [4–6], the experimental observation of the dynamo instability has long been restricted to liquid metal, requiring special care for flow optimization, and has so far been successfully realized only in the Riga [7], Karlsruhe [8], and von Kármán sodium (VKS) [9] experiments. In the latter experiment, the flow is created by the rotation of impellers within a closed cylinder. When the impellers are exactly counter-rotating, the time-averaged flow is axisymmetric and R_π symmetric—a symmetry by a rotation of angle π around any radial axis in the equatorial plane of the cylindrical container—leading to stationary axisymmetric dynamos [9,10]. In the presence of a rotation imbalance between the impellers, the forcing breaks the R_π symmetry [11,12], and various dynamical regimes have been reported, including spontaneous reversals [10,13,14]. Note that the link between symmetry breaking and magnetic field reversal has also been addressed recently in spherical shell magnetohydrodynamics (MHD) simulations [15,16]. One of the striking features of the VKS dynamos is the excitation of a time-averaged axisymmetric magnetic field, even though the Cowling theorem states that an axisymmetric fluid flow cannot sustain an axisymmetric magnetic field alone. Therefore, kinematic dynamo simulations using the time-averaged axisymmetric von Kármán flow [17–20] predicted a nonaxisymmetric equatorial dipole, dominated by an azimuthal Fourier mode $m = 1$.

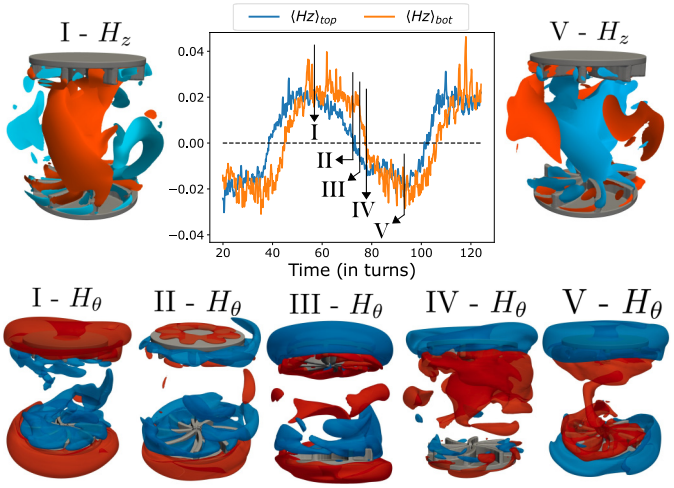

FIG. 1. Generic reversal mechanism, decomposed into five steps. Time series show the vertical magnetic field component $\langle H_z \rangle$, averaged spatially around the top impeller (blue) and the bottom impeller (orange). The impeller's turns are counted based on the slowest (bottom) one.

However, these simulations did not take into account the effect of ferromagnetic impellers that were shown to be essential for generating the observed axisymmetric dynamo mode [21–27]. Realistic simulations also demonstrated that nonferromagnetic impellers trigger the equatorial $m = 1$ dynamo mode, while increasing the impellers' magnetic permeability decreases the threshold in magnetic Reynolds number for dynamo action, and selects a dominant axisymmetric $m = 0$ magnetic mode [22,23,26].

This paper describes the mechanism of magnetic field reversals in the von Kármán sodium experiment, using numerical simulations. We present quantitative data of the spectral composition of the von Kármán MHD flow, and provide new modeling elements while linking them to previous work. Numerous simulations are performed using different boundary conditions, geometries, parameter settings, and two different solvers: LATU [22] and SFEMaNS [23]. The results are remarkably consistent between the two solvers, despite the different methods of solving the following nondimensionalized MHD equations:

$$\begin{aligned} \frac{\partial \boldsymbol{u}}{\partial t} + (\boldsymbol{u}\cdot\boldsymbol{\nabla})\boldsymbol{u} &= -\boldsymbol{\nabla}P + \frac{1}{R_e}\boldsymbol{\nabla}^2\boldsymbol{u} + \boldsymbol{\nabla}\times\boldsymbol{H}\times(\mu_r\boldsymbol{H}) + \boldsymbol{F}, \\ \frac{\partial(\mu_r\boldsymbol{H})}{\partial t} &= \boldsymbol{\nabla}\times(\boldsymbol{u}\times(\mu_r\boldsymbol{H})) - \frac{1}{R_m}\boldsymbol{\nabla}\times\left(\frac{1}{\sigma_r}\boldsymbol{\nabla}\times\boldsymbol{H}\right), \\ \boldsymbol{\nabla}\cdot\boldsymbol{u} &= 0, \quad \boldsymbol{\nabla}\cdot(\mu_r\boldsymbol{H}) = 0, \end{aligned} \tag{1}$$

where $\boldsymbol{u}$ is the velocity field, $\boldsymbol{H}$ the magnetic field, P the pressure field, and $\boldsymbol{F}$ the driving force of the impellers, realized by means of a penalty technique [28]. We denote $\sigma_r(\boldsymbol{x})$ and $\mu_r(\boldsymbol{x}, t)$ the relative electrical conductivity and magnetic permeability of the different materials involved, with $\boldsymbol{x} = (r, \theta, z)$ in cylindrical coordinates. The latter can vary in space and time to account for the use of soft iron rotating impellers, which are furthermore nonaxisymmetric (composed of a disk fitted with eight curved blades, see Fig. 1). The ratio $\Theta = (F_1 - F_2)/(F_1 + F_2)$, with F_1 and F_2 the rotation frequency of the first and second impellers driving the flow, accounts for the R_π symmetry breaking of the forcing. The dimensionless numbers controlling the dynamics are the kinetic Reynolds number $R_e = 2\pi F R_{cyl} R_{\rm imp} \nu^{-1}$ and the magnetic one $R_m = 2\pi F R_{\rm cyl} R_{\rm imp} \mu_0 \sigma$, with $F = (F_1 + F_2)/2$, ν the fluid kinematic viscosity, μ_0 the vacuum magnetic permeability, $R_{\rm cyl}$

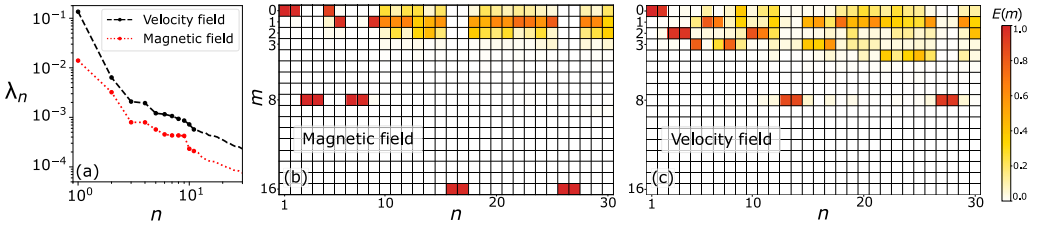

FIG. 2. (a) λ_n POD spectra of velocity and magnetic fields. Normalized azimuthal Fourier content of (b) magnetic POD modes and (c) velocity POD modes. POD modes are labeled by n and Fourier modes by m.

the vessel's radius, and R_{imp} the impellers' disk radius. It is the same setup as the experimental study of [14]. In our simulations, we address asymmetric forcings, with $F_1 > F_2$, and time is nondimensionalized by the inverse of the slowest impeller frequency, such that $t^* = 2\pi/F_2$ is one turn of the slowest impeller, then space is nondimensionalized by $R_{\text{cyl}} = 1$.

In this paper, we focus on one illustrative simulation in the LATU geometric configuration, with a conducting material layer surrounding the fluid cylinder, as described in [22]. We use the reference parameters: $R_e = 1594$, $R_m = 531$, $\Theta = 0.058$, $\mu_r = 16$ in the impellers and $\mu_r = 1$ elsewhere, with $\sigma_r = 1$. In this high-R_m, low-Θ regime, a nonoscillatory axisymmetric magnetic mode first grows before entering the reversal regime. The LATU and SFEMaNS codes also show that a strongly asymmetric forcing ($\Theta \sim 1/4$) triggers periodic reversals during the growth phase. We emphasize that a conductive surrounding medium was found to be necessary for these inversions to occur, at least within the range of parameters explored.

II. THE REVERSAL MECHANISM

First, we qualitatively describe the reversal mechanism observed in all simulations, showing the vertical H_z and azimuthal H_θ magnetic field components in Fig. 1, together with the time evolution of the mean vertical magnetic field component, $\langle H_z \rangle$, averaged spatially around the impellers, for $|z| \in [0.35, 1.2]$. Reversals can be decomposed into five distinct stages (Fig. 1). In stage I, the system exhibits a dominant magnetic dipole, with a significant H_z component in the bulk and a strong H_θ contribution near the impellers. At stage II, the magnetic field near the fastest (top) impeller is strongly weakened, and eventually changes polarity at stage III. This intermediate state corresponds to a predominantly quadrupolar structure, marked by opposite signs of H_z in the upper and lower halves of the cylinder. Stage IV is another transitional state, during which the magnetic field is reduced near the slowest (bottom) impeller. Finally, stage V restores a dipolar configuration, but with a polarity opposite to that of stage I. During the reversal, the VKS magnetic field can therefore be interpreted as the interaction of two localized dipoles, each situated near an impeller, consistent with the conceptual model of [29]. The localized dipole associated with the fastest impeller flips first, producing a temporary global quadrupole formed by the two opposing local dipoles. Afterward, the second local dipole flips, reestablishing a global dipole. The time lag between the upper and lower flips, visible in the central panel of Fig. 1, leads to a transient moving zone of weakened polarity.

III. SPECTRAL ANALYSIS OF THE FLOW

The proper orthogonal decomposition (POD) is applied to 2000 snapshots of the velocity and magnetic fields. POD modes are ordered by their energy λ_n shown in Fig. 2(a). The normalized azimuthal Fourier transform, for each POD mode n, is then displayed for the magnetic field in Fig. 2(b) and for the velocity field in Fig. 2(c) (where each POD mode n is decomposed into azimuthal modes m). For both fields, most of the energy is contained in the first pair of modes ($n = 1, 2$), which are axisymmetric, i.e., only composed of azimuthal Fourier mode $m = 0$ (Fig. 2). These four axisymmetric modes are displayed in Fig. 3, with a magnetic dipolar mode $\boldsymbol{\psi}_D(\boldsymbol{x})$

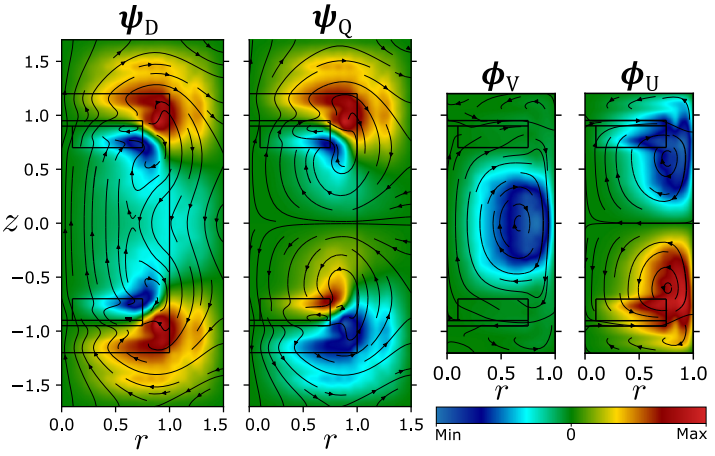

FIG. 3. Most energetic axisymmetric POD modes of the magnetic and velocity fields, with poloidal streamlines and color coding for the azimuthal component. Straight lines delimit the flow domains and the impellers.

($n = 1$), a magnetic quadrupolar mode $\boldsymbol{\psi}_Q(\boldsymbol{x})$ ($n = 2$), an R_π antisymmetric velocity mode $\boldsymbol{\phi}_V(\boldsymbol{x})$ ($n = 2$) that accounts for regimes where $\overline{\Theta} \neq 0$, and an R_π symmetric velocity $\boldsymbol{\phi}_U(\boldsymbol{x})$ ($n = 1$). In the reversal regime, the magnetic field clearly reveals the aforementioned double-dipole structure located near the impellers. The combinations $\boldsymbol{\psi}_D \pm \boldsymbol{\psi}_Q$ localize the magnetic field amplitude around one of the impellers, consistently with steps II and IV of Fig. 1. This feature was also observed in spherical shell numerical results [30] and in the VKS experiment [31]. In the Fourier-POD spectrum of $\boldsymbol{H}$ [Fig. 2(b)], the four POD modes associated with $m = 8$ contain the signature of the impellers' blades, each fitted with eight blades, and two pairs of modes are needed to localize each impeller azimuthally at $\Theta \neq 0$. Multiples of $m = 8$ modes refine the resolution of the impellers' representation subsequently, appearing again through two pairs of POD modes per Fourier mode. The magnetic POD mode $n = 5$ is composed of a $m = 0$ mode that modulates the transitional reversal states II and IV. Interestingly, there is also a pair of magnetic modes ($n = 6, n = 9$) composed only of $m = 1$, which is active all along the reversals, and is localized mainly around the impellers. Within the first few hydrodynamic POD modes, $\boldsymbol{\phi}_V$ correlates the most with reversals in the temporal domain, while modes $n = 3, 4$ correspond to Kelvin–Helmholtz vortices (with $m = 2$), reduced in number and intensity compared with the hydrodynamic flow [32]. This reduction is due to the destabilization of the equatorial shear by asymmetric forcing, and because part of the Kelvin–Helmholtz mode energy is transferred to the magnetic field. Our modal analysis highlights the key contributions of both magnetic and velocity structures, motivating a reduced-order description of the dynamics.

IV. DYNAMICS ANALYSIS AND MODELING

Modeling magnetic reversals is a long-standing topic, reviewed, e.g., in [33]. Based on the POD analysis, two pairs of modes dominate for $\boldsymbol{H}$ and $\boldsymbol{u}$:

$$\begin{aligned} \boldsymbol{H}(\boldsymbol{x}, t) &\simeq D(t)\boldsymbol{\psi}_D(\boldsymbol{x}) + Q(t)\boldsymbol{\psi}_Q(\boldsymbol{x}) \\ \boldsymbol{u}(\boldsymbol{x}, t) &\simeq V(t)\boldsymbol{\phi}_V(\boldsymbol{x}) + U(t)\boldsymbol{\phi}_U(\boldsymbol{x}). \end{aligned} \tag{2}$$

The dipole $D(t)$ and quadrupole $Q(t)$ magnetic modes evolve on similar timescales, as shown in Fig. 4. The zonal velocity mode $V(t)$ fluctuates around a small positive mean, and undergoes large deviations on a slow timescale corresponding to a reversing magnetic field. The symmetric velocity mode $U(t)$ remains close to its large mean value, with small fluctuations, and correlates strongly with $V(t)$ when the latter flips sign during a magnetic inversion. Magnetic modes $n = 3$ and $n = 7$,

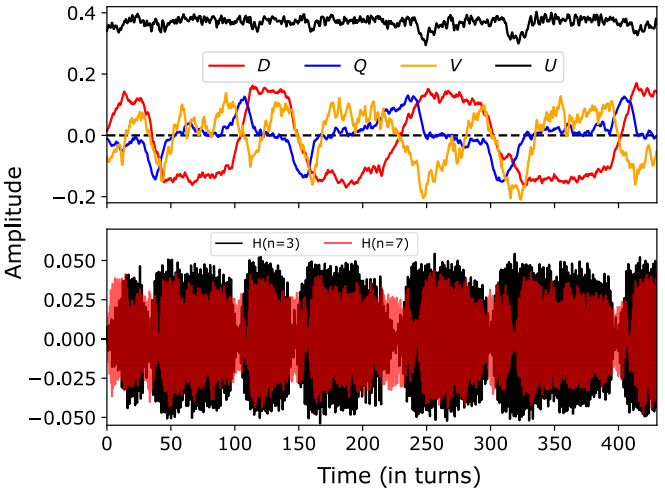

FIG. 4. Top: timeseries of the four main modes involved in the reversal dynamics; $D(t)$, $Q(t)$, $V(t)$, $U(t)$. Bottom: timeseries of magnetic modes $n = 3$ and $n = 7$, that are localized around the upper and lower impeller, respectively.

composed exclusively of Fourier mode $m = 8$ (see Fig. 2), represent the interblades magnetic field, as studied in [34–36]. They are localized around the upper and lower impeller, and time series (Fig. 4) show that they cancel to zero when the axisymmetric magnetic field is in a state $D - Q$ and $D + Q$, respectively. This is again consistent with the described mechanism: during reversals, the magnetic field localizes on one half of the cylinder.

Dynamical equations of the time coefficients are obtained after injecting the system (2) into the MHD equations (1), first projecting the induction equation onto $\boldsymbol{\psi}_D$ and $\boldsymbol{\psi}_Q$, then projecting the Navier-Stokes equation onto $\boldsymbol{\phi}_V$ and $\boldsymbol{\phi}_U$. Integrating over space yields a Galerkin model, in which most integrals cancel due to symmetry. There is indeed a double constraint on the allowed couplings with the Fourier triadic interaction rule and the need for an even number of R_π antisymmetric terms within a given triad. This Galerkin model can be expressed as follows:

$$\begin{pmatrix}\dot{D}\\ \dot{Q}\end{pmatrix} = \begin{pmatrix}\Omega_{dud}U + \alpha_d + \frac{\mathcal{L}_d}{Rm} & \Omega_{dvq}V + \omega_d \\ \Omega_{qvd}V + \omega_q & \Omega_{quq}U + \alpha_q + \frac{\mathcal{L}_q}{Rm}\end{pmatrix} \cdot \begin{pmatrix}D\\ Q\end{pmatrix},$$

$$\dot{V} = \gamma_-(t) + \frac{L_v}{Re}V - A_{vuv}UV + T_{vdq}DQ,$$

$$\dot{U} = \gamma_+(t) + \frac{L_u}{Re}U - A_{uvv}V^2 + T_{udd}D^2 + T_{uqq}Q^2, \tag{3}$$

where the constant parameters are resulting from the spatial integration of the inertial terms (A_{ijk}), the Lorentz force terms (T_{ijk}), the Ohm's law terms (Ω_{ijk}), and the Joule ($\mathcal{L}_i$) and viscous (L_i) diffusion terms. Furthermore, we added the time-dependent parameters $\alpha_i(t)$ and $\omega_i(t)$ to represent the effect of all the other modes on D and Q, whilst the terms $\gamma_\pm(t)$ represent the hydrodynamic forcing from the impellers. To further simplify, we make use of the separation between the slow timescale of the magnetic field and the fast timescale of the velocity field to assume that α_i and ω_i can be regarded as constants with respect to D and Q. We define effective coefficients (the time average is denoted $\langle\cdot\rangle$),

$$\bar{\alpha_i} = \langle\alpha_i(t)\rangle + \frac{\mathcal{L}_i}{Rm},\ i \in \{d, q\}, \tag{4}$$

$$\bar{\omega_i} = \langle\omega_i(t)\rangle = 0, \tag{5}$$

and finally decide to completely neglect ω_i, to account for coupling between D and Q only through V. One can justify the latter approximation considering that V holds most of the R_π antisymmetric energy of the fluid, expressed by the condition: $\bar{V} = \langle V(t)\rangle \gg \bar{\omega}_i$. We also consider constant forcing, $\bar{\gamma}_\pm = \langle \gamma_\pm(t)\rangle$. These approximations lead to the simplified dynamics,

$$\begin{aligned}
\dot{D} &= \bar{\alpha}_d D + \Omega_{dud} U D + \Omega_{dvq} V Q,\\
\dot{Q} &= \bar{\alpha}_q Q + \Omega_{quq} U Q + \Omega_{qvd} V D,\\
\dot{V} &= \bar{\gamma}_- + \frac{L_v}{Re} V - A_{vvu} V U + T_{vdq} D Q,\\
\dot{U} &= \bar{\gamma}_+ + \frac{L_u}{Re} U - A_{uvv} V^2 + T_{udd} D^2 + T_{uqq} Q^2.
\end{aligned} \tag{6}$$

Moreover, if we eliminate U by applying the same averaging procedure as for α_i and define

$$\bar{\beta}_i = \bar{\alpha}_i + \Omega_{iui}\langle U(t)\rangle, \tag{7}$$

$$\bar{\alpha}_v = \frac{L_v}{Re} - A_{vuv}\langle U(t)\rangle, \tag{8}$$

we obtain exactly the DQV model studied in [37,38]:

$$\begin{aligned}
\dot{D} &= \bar{\beta}_d D + \Omega_{dvq} V Q,\\
\dot{Q} &= \bar{\beta}_q Q + \Omega_{qvd} V D,\\
\dot{V} &= \bar{\gamma}_- + \bar{\alpha}_v V + T_{vdq} D Q.
\end{aligned} \tag{9}$$

V. MODEL'S IDENTIFICATION

Having derived the governing equations for candidate dynamical models, we now assess their relative performance in characterizing the observed simulation. The objective is to evaluate to what extent these reduced-order models can provide sufficient complexity to capture the underlying system dynamics. To facilitate this comparison and to avoid delving into the complexity of $\alpha_i(t)$, which incorporates contributions from various modes of the spectrum, the model parameters are estimated from time series data using a constrained Galerkin regression framework, as proposed in [39]. In particular, we enforce the Navier-Stokes quadratic constraint in the $DQVU$ model:

$$A_{uvv} + A_{vvu} = 0. \tag{10}$$

We do not constrain the system to conserve exactly the energy, because it would be conserving an underestimated value since we truncated the full system to three or four modes. Instead, we choose to statistically conserve the third moment, in order to favor asymmetric distributions on $V(t)$ and $U(t)$, as visible on Fig. 4. Denoting the reduced system by $\dot{X} = f(X, p)$, with f defined by Eqs. (6) or (9), p the list of model's parameters, and $X = (D, Q, V)^T$ or $X = (D, Q, V, U)^T$, we impose

$$\langle X^2 \cdot f(X, p)\rangle = 0. \tag{11}$$

This constraint has proved useful in identifying models with asymmetric distributions, thereby compensating in practice for the lack of data. Finally, we solve the following problem using the PySINDy framework [40]:

$$p\star = \arg\min_p \left\{ ||\dot{X} - f(X, p)||_2^2 + \kappa ||C(p)||_2^2 \right\}, \tag{12}$$

where the vector C encodes the linear constraints on the parameters p, defined by Eqs. (10) and (11), with $\kappa < 1$. The ability to obtain pertinent model parameters from data using this method

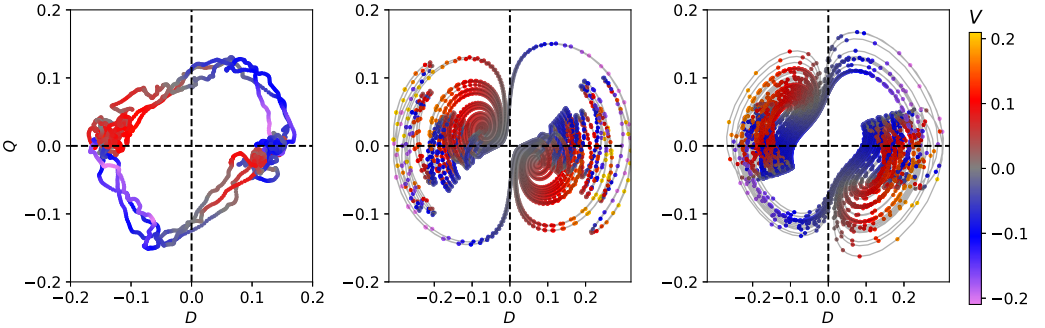

FIG. 5. (D, Q) plane. Left: DNS; center: DQV model; right: $DQVU$ model.

depends strongly on the proper evaluation of the time derivatives. To mitigate the issue that the high frequencies are not fully resolved in our time series, we use a Savitzky–Golay filter on $\dot{X}$, whose relevance to our context has been documented in [41]. These constraints are sufficient to ensure that the models remain stable during time integration and reproduce the main characteristics of the observed data. Then, we explore systematically the set of models around the ones found by solving the optimization problem, and select the best ones. It should be noted that, of all the models that fit the data well and have a low error, only a few are stable during time integration, and even fewer have distributions that match the data. Adding constraints helps identify stable models, while understanding the model's parameters is needed to shape the system manifold and obtain the correct distributions. The (D, Q) phase portraits comparing the data with trajectories computed from the identified DQV and $DQVU$ models are shown in Fig. 5. In this representation, the simulation data agree well with the experimental data presented in [42]. The coefficients used to compute the trajectories of Fig. 5 are reported in the Appendix (Tables I and II).

As observed during the exploration of the different models, the DQV model offers limited flexibility in localizing its fixed points along the D axis, so that the dominant states are where $D^\star \neq 0$ is large and $Q^\star = 0$. In fact, the DQV models that best represent the system dynamics tend to position these dominant states along the diagonal, where $D^\star = \pm Q^\star$. In contrast, the $DQVU$ model allows greater freedom in localizing these fixed points, due to the additional variable U, which also interacts on a fast timescale with V and strongly affects its dynamics. This distinction is clearly reflected in the statistical distributions: the distribution of V in the DQV model is highly peaked, whereas the empirical data show a nonsymmetric bimodal distribution. The $DQVU$ model successfully reproduces this bimodality, see Fig. 6, demonstrating that the temporal dependence of the source term for V, modeled here as a weakened UV coupling during inversions, is essential for accurately capturing the dynamics of V and, by extension, the magnetic field's dynamics. The couplings with U also seem necessary to obtain the reversal mechanism correctly, with transition states $D = \pm Q$, whereas in the DQV model, reversals typically occur along the $D = 0$ axis. The distribution of D is also more accurately reproduced by the $DQVU$ model, despite a slight degradation in the fit for the Q distribution, where only the main peak width is well captured. In summary, these models are capable of capturing the main characteristics of the full-order simulation, but with only three or four dynamical variables, providing simplified yet valuable insights into the parameters that influence the global structure of the manifold on which the system evolves.

Beyond understanding the need for a velocity mode that breaks the system's symmetry in order to couple the symmetric and antisymmetric magnetic modes, the more general picture is to understand how this symmetry breaking occurs in various MHD systems. In this context, the von Kármán flow is a useful case to consider, since, on the one hand, it is possible to control the extent of the symmetry breaking by varying the forcing parameter Θ, and, on the other hand, the dynamics of the generated V mode may be nontrivial, as it is coupled to the rapid dynamics of the velocity field.

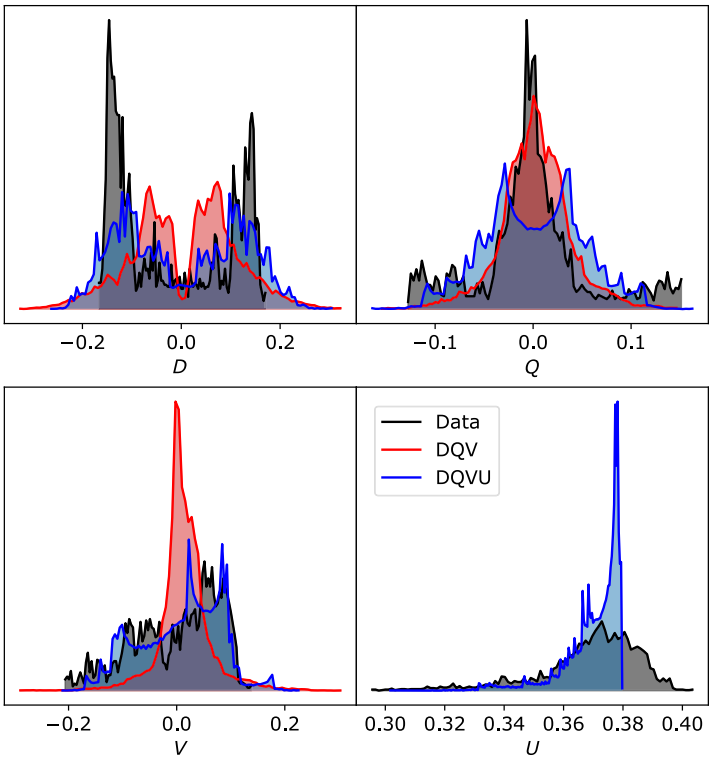

FIG. 6. Distributions of the modeled time coefficients.

A natural extension of the presented model should be to couple explicitly the axisymmetric modes considered here with nonaxisymmetric modes, in particular with the Kelvin–Helmholtz instability modes, which are known to be linked to V through the angular momentum budget [32].

VI. CONCLUSION

Numerical simulations are presented in the VKS geometry using two different solvers. It was observed that a surrounding conducting material is necessary to achieve magnetic field reversals within the range of parameters explored. The reversal mechanism has been analyzed in detail with a modal analysis using proper orthogonal decomposition, which revealed that the dynamics are dominated by two magnetic modes (dipolar and quadrupolar) and two velocity modes (zonal and R_π symmetric). This justifies the use of a reduced-order Galerkin model derived from the full MHD equations, capturing the principal features of the reversal dynamics. The general development of the MHD equations is simplified in the framework of a system with four degrees of freedom, leading to a new model ($DQVU$) that reduces to a three-variable model (DQV), previously derived from symmetry considerations. This $DQVU$ model represents a significant step forward, as it introduces greater complexity into the velocity field, which is necessary to reproduce certain fundamental characteristics of the magnetic field dynamics.

ACKNOWLEDGMENTS

The authors acknowledge the support of the Agence Nationale de la Recherche (ANR) through the MilaDy project (Grant No. ANR-25-CE51-0077-02) and the IDEX of Université Côte d'Azur

TABLE I. Values of the parameters and initial condition used for the DQVU system.

D coefficients	Q coefficients
$\bar{\alpha}_d = 3.9988 \times 10^{-2}$	$\bar{\alpha}_q = -2.5179 \times 10^{-1}$
$\Omega_{dud} = -1.2961 \times 10^{-1}$	$\Omega_{quq} = 1.2639 \times 10^{-1}$
$\Omega_{dvq} = -5.5429 \times 10^{-1}$	$\Omega_{qvd} = 7.0752 \times 10^{-1}$
V coefficients	U coefficients
$\bar{\gamma}_- = -7.2694 \times 10^{-4}$	$\bar{\gamma}_+ = 1.7228 \times 10^{-1}$
$\frac{L_v}{Re} = -2.8870 \times 10^{-1}$	$\frac{L_u}{Re} = -4.5456 \times 10^{-1}$
$A_{vvu} = 7.3282 \times 10^{-1}$	$A_{uvv} = -7.3282 \times 10^{-1}$
$T_{vdq} = -7.1738 \times 10^{-1}$	$T_{udd} = -1.8434 \times 10^{-2}$
	$T_{uqq} = -1.4143 \times 10^{-1}$
Initial conditions	
$D_0 = -1.19801 \times 10^{-1}$	$Q_0 = 5.7068 \times 10^{-2}$
$V_0 = 9.3942 \times 10^{-2}$	$U_0 = 3.6550 \times 10^{-1}$

(Grant No. ANR-15-IDEX-01). The authors also acknowledge the use of HPC resources from GENCI (Grants No. AD012A01357R3 and No. A0182A00254) and the Université Côte d'Azur's Center for High-Performance Computing (OPAL infrastructure) for providing resources and support.

DATA AVAILABILITY

The data that support the findings of this article are not publicly available upon publication because it is not technically feasible and/or the cost of preparing, depositing, and hosting the data would be prohibitive within the terms of this research project. The data are available from the authors upon reasonable request.

APPENDIX: FITTED MODEL PARAMETERS

The following Tables I and II list the fitted parameter values obtained from the data, which are used to integrate in time the models of Eqs. 6 and 9, respectively.

TABLE II. Values of the parameters and initial condition used for the DQV system.

D coefficients	Q coefficients
$\bar{\beta}_d = -5.2356 \times 10^{-3}$	$\bar{\beta}_q = 1.2721 \times 10^{-2}$
$\Omega_{dvq} = -5.0420 \times 10^{-1}$	$\Omega_{qvd} = 1.4953 \times 10^{-1}$
V coefficients	Initial conditions
$\bar{\gamma}_- = 2.3070 \times 10^{-4}$	$D_0 = -1.1980 \times 10^{-1}$
$\bar{\alpha}_v = -2.7315 \times 10^{-2}$	$Q_0 = 5.7068 \times 10^{-2}$
$T_{vdq} = -6.3774 \times 10^{-1}$	$V_0 = 9.3942 \times 10^{-2}$

[1] F. Rincon, Dynamo theories, J. Plasma Phys. **85**, 205850401 (2019).
[2] S. Tobias, The turbulent dynamo, J. Fluid Mech. **912**, P1 (2021).
[3] C. C. Finlay, C. Kloss, and N. Gillet, Core field changes from eleven years of *Swarm* satellite observations, Phys. Earth Planet. Inter. **368**, 107447 (2025).
[4] P. Tzeferacos, A. Rigby, A. F. A. Bott, A. R. Bell, R. Bingham, A. Casner, F. Cattaneo, E. M. Churazov, J. Emig, F. Fiuza, C. B. Forest, J. Foster, C. Graziani, J. Katz, M. Koenig, C.-K. Li, J. Meinecke, R. Petrasso, H.-S. Park, B. A. Remington, *et al.*, Laboratory evidence of dynamo amplification of magnetic fields in a turbulent plasma, Nat. Commun. **9**, 591 (2018).
[5] A. F. A. Bott, P. Tzeferacos, L. Chen, C. A. J. Palmer, A. Rigby, A. R. Bell, R. Bingham, A. Birkel, C. Graziani, D. H. Froula, J. Katz, M. Koenig, M. W. Kunz, C. Li, J. Meinecke, F. Miniati, R. Petrasso, H.-S. Park, B. A. Remington, B. Reville, *et al.*, Time-resolved turbulent dynamo in a laser plasma, Proc. Natl. Acad. Sci. USA **118**, e2015729118 (2021).
[6] A. F. A. Bott, L. Chen, P. Tzeferacos, C. A. J. Palmer, A. R. Bell, R. Bingham, A. Birkel, D. H. Froula, J. Katz, M. W. Kunz, C.-K. Li, H.-S. Park, R. Petrasso, J. S. Ross, B. Reville, D. Ryu, F. H. Séguin, T. G. White, A. A. Schekochihin, D. Q. Lamb, *et al.*, Insensitivity of a turbulent laser-plasma dynamo to initial conditions, Matter Radiat. Extremes **7**, 046901 (2022).
[7] A. Gailitis, O. Lielausis, S. Dement'ev, E. Platacis, A. Cifersons, G. Gerbeth, T. Gundrum, F. Stefani, M. Christen, H. Hänel, and G. Will, Detection of a flow induced magnetic field eigenmode in the Riga dynamo facility, Phys. Rev. Lett. **84**, 4365 (2000).
[8] R. Stieglitz and U. Müller, Experimental demonstration of a homogeneous two-scale dynamo, Phys. Fluids **13**, 561 (2001).
[9] R. Monchaux, M. Berhanu, M. Bourgoin, M. Moulin, P. Odier, J.-F. Pinton, R. Volk, S. Fauve, N. Mordant, F. Pétrélis, A. Chiffaudel, F. Daviaud, B. Dubrulle, C. Gasquet, L. Marié, and F. Ravelet, Generation of a magnetic field by dynamo action in a turbulent flow of liquid sodium, Phys. Rev. Lett. **98**, 044502 (2007).
[10] R. Monchaux, M. Berhanu, S. Aumaître, A. Chiffaudel, F. Daviaud, B. Dubrulle, F. Ravelet, S. Fauve, N. Mordant, F. Pétrélis, M. Bourgoin, P. Odier, J.-F. Pinton, N. Plihon, and R. Volk, The von Kármán Sodium experiment: Turbulent dynamical dynamos, Phys. Fluids **21**, 035108 (2009).
[11] F. Ravelet, L. Marié, A. Chiffaudel, and F. Daviaud, Multistability and memory effect in a highly turbulent flow: Experimental evidence for a global bifurcation, Phys. Rev. Lett. **93**, 164501 (2004).
[12] P.-P. Cortet, P. Diribarne, R. Monchaux, A. Chiffaudel, F. Daviaud, and B. Dubrulle, Normalized kinetic energy as a hydrodynamical global quantity for inhomogeneous anisotropic turbulence, Phys. Fluids **21**, 025104 (2009).
[13] M. Berhanu, R. Monchaux, S. Fauve, N. Mordant, F. Pétrélis, A. Chiffaudel, F. Daviaud, B. Dubrulle, L. Marié, F. Ravelet, M. Bourgoin, P. Odier, J.-F. Pinton, and R. Volk, Magnetic field reversals in an experimental turbulent dynamo, Europhys. Lett. **77**, 59001 (2007).
[14] M. Berhanu, G. Verhille, J. Boisson, B. Gallet, C. Gissinger, S. Fauve, N. Mordant, F. Pétrélis, M. Bourgoin, P. Odier, J.-F. Pinton, N. Plihon, S. Aumaître, A. Chiffaudel, F. Daviaud, B. Dubrulle, and C. Pirat, Dynamo regimes and transitions in the VKS experiment, Eur. Phys. J. B **77**, 459 (2010).
[15] N. P. Müller, C. Gissinger, and F. Pétrélis, Magnetic reversals in a geodynamo model with a stably–stratified layer, Phys. Earth Planet. Inter. **371**, 107502 (2026).
[16] P. Barrère, J. Guilet, B. Gallet, and R. Raynaud, Complex dynamical regimes of the Tayler-Spruit dynamo, arXiv:2601.02182 .
[17] F. Ravelet, A. Chiffaudel, F. Daviaud, and J. Léorat, Toward an experimental von Kármán dynamo: Numerical studies for an optimized design, Phys. Fluids **17**, 117104 (2005).
[18] F. Stefani, M. Xu, G. Gerbeth, F. Ravelet, A. Chiffaudel, F. Daviaud, and J. Léorat, Ambivalent effects of added layers on steady kinematic dynamos in cylindrical geometry: Application to the VKS experiment, Eur. J. Mech. B. Fluids **25**, 894 (2006).
[19] R. Laguerre, C. Nore, J. Léorat, and J.-L. Guermond, Effects of conductivity jumps in the envelope of a kinematic dynamo flow, Comptes Rendus. Mécanique **334**, 593 (2006).
[20] A. Pinter, B. Dubrulle, and F. Daviaud, Kinematic dynamo simulations of von Kármán flows: application to the VKS experiment, Eur. Phys. J. B **74**, 165 (2010).

[21] S. Miralles, N. Bonnefoy, M. Bourgoin, P. Odier, J.-F. Pinton, N. Plihon, G. Verhille, J. Boisson, F. Daviaud, and B. Dubrulle, Dynamo threshold detection in the von Kármán sodium experiment, Phys. Rev. E **88**, 013002 (2013).
[22] S. Kreuzahler, Y. Ponty, N. Plihon, H. Homann, and R. Grauer, Dynamo enhancement and mode selection triggered by high magnetic permeability, Phys. Rev. Lett. **119**, 234501 (2017).
[23] C. Nore, D. Castanon Quiroz, L. Cappanera, and J.-L. Guermond, Numerical simulation of the von Kármán sodium dynamo experiment, J. Fluid Mech. **854**, 164 (2018).
[24] R. Laguerre, C. Nore, A. Ribeiro, J. Léorat, J.-L. Guermond, and F. Plunian, Impact of impellers on the axisymmetric magnetic mode in the VKS2 dynamo experiment, Phys. Rev. Lett. **101**, 104501 (2008).
[25] A. Giesecke, C. Nore, F. Stefani, G. Gerbeth, J. Léorat, W. Herreman, F. Luddens, and J.-L. Guermond, Influence of high-permeability discs in an axisymmetric model of the Cadarache dynamo experiment, New J. Phys. **14**, 053005 (2012).
[26] M. Creff, H. Faller, B. Dubrulle, J.-L. Guermond, and C. Nore, Tracking dynamo mechanisms from local energy transfers: Application to the von Kármán sodium dynamo, Phys. Plasmas **31**, 022306 (2024).
[27] V. Botez, R. Bousquet, and C. Nore, Large scale analysis of the von Kármán sodium experiment using proper orthogonal decomposition, Magnetohydrodynamics **61**, 13 (2025).
[28] R. Pasquetti, R. Bwemba, and L. Cousin, A pseudo-penalization method for high Reynolds number unsteady flows, Appl. Numer. Math. **58**, 946 (2008).
[29] N. Plihon, S. Miralles, M. Bourgoin, and J.-F. Pinton, Stochastic reversal dynamics of two interacting magnetic dipoles: A simple model experiment, Phys. Rev. E **94**, 012224 (2016).
[30] B. Gallet and F. Pétrélis, From reversing to hemispherical dynamos, Phys. Rev. E **80**, 035302(R) (2009).
[31] B. Gallet, S. Aumaître, J. Boisson, F. Daviaud, B. Dubrulle, N. Bonnefoy, M. Bourgoin, P. Odier, J.-F. Pinton, N. Plihon, G. Verhille, S. Fauve, and F. Pétrélis, Experimental observation of spatially localized dynamo magnetic fields, Phys. Rev. Lett. **108**, 144501 (2012).
[32] R. Bousquet, O. Chaffard, M. Creff, D. Lucor, and C. Nore, Large scale analysis of three-dimensional turbulent von Kármán swirling flows, Phys. Fluids **36**, 105133 (2024).
[33] F. Pétrélis and S. Fauve, Mechanisms for magnetic field reversals, Philos. Trans. R. Soc. A **368**, 1595 (2010).
[34] F. Ravelet, B. Dubrulle, F. Daviaud, and P.-A. Ratié, Kinematic α tensors and dynamo mechanisms in a von Kármán swirling flow, Phys. Rev. Lett. **109**, 024503 (2012).
[35] J. Varela, S. Brun, B. Dubrulle, and C. Nore, Role of boundary conditions in helicoidal flow collimation: Consequences for the von Kármán sodium dynamo experiment, Phys. Rev. E **92**, 063015 (2015).
[36] C. J. P. Gissinger, A numerical model of the VKS experiment, EPL (Europhysics Letters) **87**, 39002 (2009).
[37] C. Gissinger, E. Dormy, and S. Fauve, Morphology of field reversals in turbulent dynamos, EPL (Europhysics Letters) **90**, 49001 (2010).
[38] C. Gissinger, A new deterministic model for chaotic reversals, Eur. Phys. J. B **85**, 137 (2012).
[39] J.-C. Loiseau and S. L. Brunton, Constrained sparse Galerkin regression, J. Fluid Mech. **838**, 42 (2018).
[40] A. Kaptanoglu, B. de Silva, U. Fasel, K. Kaheman, A. Goldschmidt, J. Callaham, C. Delahunt, Z. Nicolaou, K. Champion, J.-C. Loiseau, J. Kutz, and S. Brunton, PySINDy: A comprehensive Python package for robust sparse system identification, J. Open Source Software **7**, 3994 (2022).
[41] F. V. Van Breugel, J. N. Kutz, and B. W. Brunton, Numerical differentiation of noisy data: A unifying multi-objective optimization framework, IEEE Access **8**, 196865 (2020).
[42] C. Gissinger, Dipole-quadrupole dynamics during magnetic field reversals, Phys. Rev. E **82**, 056302 (2010).